Self-Driven WSe$_2$/Bi$_2$O$_2$Se Van der Waals Heterostructure Photodetectors with High Light On/Off Ratio and Fast Response

Peng Luo, Fakun Wang, Jingyu Qu, Kailang Liu, Xiaozong Hu, Kewei Liu, and Tianyou Zhai*

Benefiting from the superior electron mobility and good air-stability, the emerging layered bismuth oxyselenide (Bi$_2$O$_2$Se) nanosheet has received considerable attention with the promising prospects for electronics and opto-electronics applications. However, the high charge carrier concentration and bolometric effect of Bi$_2$O$_2$Se give rise to the high dark current and relatively slow photoresponse, which severely impede further improvement of the performance of Bi$_2$O$_2$Se based photodetectors. Here, a WSe$_2$/Bi$_2$O$_2$Se Van der Waals p-n heterostructure is reported with a pronounced rectification ratio of 10^5 and a low reverse dark current of 10^{-11} A, as well as an enhanced light on/off ratio up to 618 under 532 nm light illumination. The device also exhibits a fast response speed of 2.6 µs and a broadband detection capability from 365 to 2000 nm due to the efficient charge separation and strong interlayer coupling at the interface of the two flakes. Importantly, the built-in potential in the WSe$_2$/Bi$_2$O$_2$Se heterostructure offers a competitive self-powered photo-detector with the light on/off ratio above 10^5 and a photovoltaic responsivity of 284 mA W^{-1}. The WSe$_2$/Bi$_2$O$_2$Se heterostructure shows promising potentials for high-performance self-driven photodetector applications.

1. Introduction

2D materials as the superior candidates for next-generation electronics and optoelectronics integrated devices are drawing increasing attention for their unique confined structure and abundant properties.[1–4] Numerous efforts have been devoted to predict and prepare new 2D materials, facilitating the rapidly growing family of 2D materials including graphene,[5–7] black phosphorus (BP),[8–10] perovskite,[11–13] and transition metal dichalcogenides.[14,15] Very recently, a new 2D semiconductor Bi$_2$O$_2$Se reported by Peng et al. has gained wide interest due to its excellent electron mobility and good ambient stability.[16,17] Tremendous progress has been achieved in the structural analysis,[17–19] controlled synthesis,[20–23] precision etching,[24] non-corrosive transfer,[23,25] and large area growth[26,27] of 2D Bi$_2$O$_2$Se, which paved the way for advanced electronics and optoelectronics device applications.[28–31] The 2D Bi$_2$O$_2$Se exhibits an ultra-high mobility ($\approx$20 000 cm^2 V^{-1} s^{-1}) comparable to graphene and proper band gap of 0.8 eV, it is thus worth exploring its merits in high-performance photodetection applications.[22,25,32–36] For example, Liu et al. fabricated ultrasensitive phototransistors based on Bi$_2$O$_2$Se nanosheets with a responsivity and a detectivity up to 3.5 × 10^4 A W^{-1} and 9.0 × 10^{13} Jones, respectively, which were among the best performance of 2D materials photodetector.[25] Xu et al. achieved a sensitive and broadband phototransistor for 360–1800 nm based on high-quality CVD-grown Bi$_2$O$_2$Se nanosheets.[35] More recently, our group expanded the detection range of 2D Bi$_2$O$_2$Se up to 2 µm with a responsivity greater than 10^3 A W^{-1} by combining with the PbSe colloidal quantum dots.[34] However, the high dark current (>10^{-7} A at 1 V) and relatively slow photoresponse ($\approx$ms) caused by the high charge carrier concentration ($\approx$10^{18}–10^{20} cm^{-3})[34] and bolometric effect[36] have become obstacles for further development of high optical on/off ratio and fast response Bi$_2$O$_2$Se photodetectors. Although several attempts have been made to alleviate such bottleneck through the optimizations of synthesis process[21] and regulation of gate voltage,[22,25] effective reduction of the dark current of 2D Bi$_2$O$_2$Se with a simple configuration and low power consumption remains challenging.

Toward this end, we design a Van der Waals (vdW) vertical heterostructure to regulate the photoelectric performance of 2D Bi$_2$O$_2$Se by manually stacking suitable materials. Taking advantage of the type II staggered band alignment p-n junction,

P. Luo, F. K. Wang, Dr. J. Y. Qu, Dr. K. L. Liu, Dr. X. Z. Hu, Prof. T. Y. Zhai
State Key Laboratory of Materials Processing
and Die & Mould Technology
School of Materials Science and Engineering
Huazhong University of Science and Technology (HUST)
Wuhan 430074, P. R. China
E-mail: zhaity@hust.edu.cn
Dr. X. Z. Hu
Green Catalysis Center, and College of Chemistry
Zhengzhou University
Zhengzhou 450001, P. R. China
Prof. K. W. Liu
State Key Laboratory of Luminescence and Applications
Changchun Institute of Optics
Fine Mechanics and Physics
Chinese Academy of Science
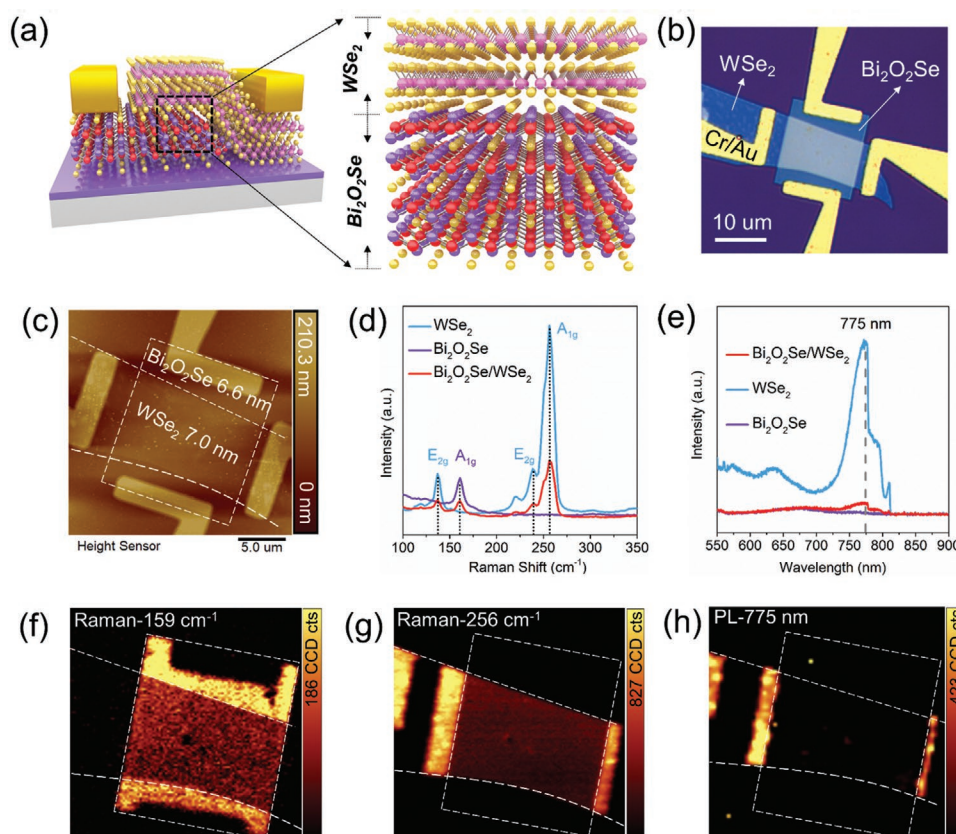Changchun 130033, P. R. China

Figure 1. Characterization of WSe₂/Bi₂O₂Se heterostructure. a) Schematics illustration of WSe_2/Bi_2O_2Se heterostructure device. b,c) Optical image and AFM image of the fabricated WSe_2/Bi_2O_2Se heterostructure. d,e) Raman and PL spectra of the WSe_2/Bi_2O_2Se heterostructure, individual WSe_2 and Bi_2O_2Se. f,g) Raman mapping images for Bi_2O_2Se and WSe_2, respectively. h) PL mapping image for WSe_2.

the channel current can be greatly suppressed by the interface potential barrier in the dark state, and the electrons and holes are likely to transit to different materials rapidly under light stimulation.[37,38] Therefore, we construct a Bi_2O_2Se based 2D/2D vdW p-n heterostructure with p-dominant ambipolarity semiconductor WSe_2 due to its desirable band gap and outstanding photoelectric properties (**Figure 1**a).[39,40] Ultraviolet photoelectron spectra (UPS) evidenced the proposed type II band alignment, the Raman and photoluminescence (PL) measurements further confirmed the strong interlayer coupling and efficient charge transfer at the WSe_2/Bi_2O_2Se interface. The low reverse current about 10^{-11} A and the high rectification ratio of 10^5 indicated a large potential barrier in our WSe_2/Bi_2O_2Se heterostructure, which contributed to a high sensitivity photodiode with a great light on/off ratio up to 618 and the high responsivity of 638 mA W^{-1} under 532 nm light. Continuous and stable photoresponse from 365 to 2000 nm indicated the promising potential application in broadband photodetection of the heterostructure. The type II interfacial band offset between WSe_2 and Bi_2O_2Se sped up the response time to 2.6 µs, which was much faster than other Bi_2O_2Se devices.[25,32,34,36] Furthermore, the self-driven photodetection was first achieved in WSe_2/Bi_2O_2Se heterostructure with a photovoltaic responsivity of 284 mA W^{-1} and a light on/off ratio up to 10^5 at room temperature (10^6 at 77 K). Our results suggest that the WSe_2/Bi_2O_2Se heterostructure offers a simple yet effective approach to realize low dark current, fast response, broadband, and self-driven photodetectors.

2. Results and Discussion

2.1. Characterization of WSe₂/Bi₂O₂Se Heterostructure

To construct the WSe_2/Bi_2O_2Se heterostructure, we first synthesized the few-layer Bi_2O_2Se nanosheets on freshly cleaved fluorophlogopite mica $[KMg_3(AlSi_3O_{10})F_2]$ through chemical vapor deposition (CVD) as previously reported[20,34] and transferred them to SiO_2/Si substrate by the wet transfer method.[18] The multilayer WSe_2 nanosheets were mechanically exfoliated on the transparent stamp poly (dimethylsiloxane) (PDMS) and target-transferred on the top of the prepared Bi_2O_2Se nanosheet as shown in Figure S1a, Supporting Information (more details can be found in Experimental Section). Figure 1b illustrates the optical microscope (OM) image of a typical heterostructure device on SiO_2/Si substrate with the Cr/Au (5/50 nm) electrodes on the separated Bi_2O_2Se and WSe_2. The thicknesses of the CVD synthesized Bi_2O_2Se and mechanically exfoliated WSe_2 nanosheets were about 6.6 nm (≈10 layers) and 7.0 nm (≈11 layers), respectively, as confirmed by the atomic force microscopy (AFM) (Figure 1c and Figure S1b, Supporting Information).
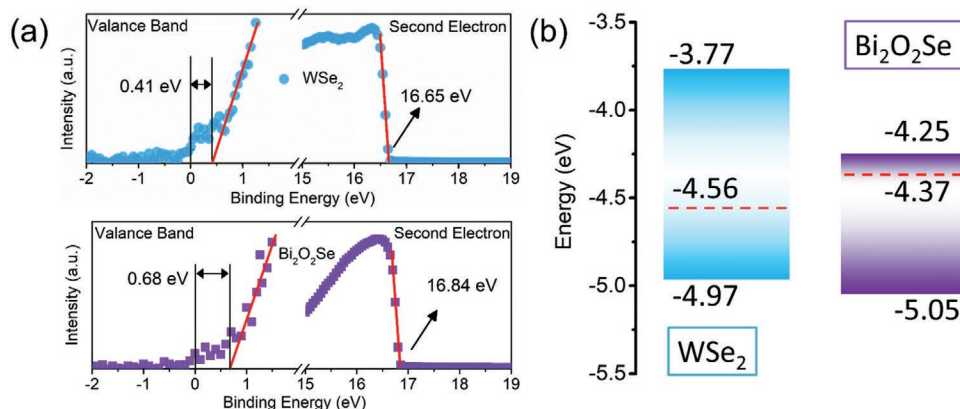
Figure 2. The band alignment of WSe_2/Bi_2O_2Se heterostructure. a) Ultraviolet photoelectron spectra of WSe_2 and Bi_2O_2Se for work function and valence band edge. b) Band alignment of WSe_2/Bi_2O_2Se heterostructure before contact.

The coupling effect and charge transfer at WSe_2/Bi_2O_2Se interface can be verified via the optical measurements.[40] The Raman spectra collected from isolated WSe_2, Bi_2O_2Se, and the overlapped junction are exhibited in Figure 1d. No obvious shift was observed for the characteristic peaks in the overlapped heterostructure region, indicating high quality of the vdW heterostructure after the wet transfer, exfoliation, and target-transfer processes.[41] Apparent reduction of Raman intensity called "Raman quench" indicated a strong interfacial coupling between the two flakes.[40,42,43] The Raman mapping of Bi_2O_2Se (159 cm^{-1}) and WSe_2 (256 cm^{-1}) (Figure 1f,g) further confirms the high-quality of the heterostructure, exhibiting a great homogeneity of each component. We also collected the PL spectra from different areas (Figure 1e) and found no obvious PL signal was observed for bare Bi_2O_2Se due to the intrinsic indirect optical bandgap,[18,20] but strong excitonic emission around 775 nm of bare WSe_2.[40] Similar quenching effect of PL can also be clearly observed at the heterostructure area (Figure 1e,h), indicating the efficient separation and transition of photogenerated electrons and holes, which resulted in the increase of non-radiative recombination and the decrease of PL emission recombination.[44]

2.2. The Band Alignment of WSe_2/Bi_2O_2Se Heterostructure

The charge transport behavior at vdW heterostructure is intrinsically determined by the energy band.[37,42] We thus carried out the UPS measurement to obtain the energy band alignment of the WSe_2/Bi_2O_2Se heterostructure as seen in **Figure 2**a. The work functions (W) of WSe_2 and Bi_2O_2Se were determined to be 4.56 and 4.37 eV, respectively, by subtracting the second electron cutoff energy from the photo energy of He I light source (21.21 eV).[34] The valence band edges of WSe_2 and Bi_2O_2Se were 0.41 and 0.68 eV, lower than their Fermi level (F_E) (binding energy equals to 0 eV). Therefore, a type II band alignment was suggested in Figure 2b if we take the bandgap of multilayer WSe_2 and Bi_2O_2Se to be 1.2 and 0.8 eV.[34,45] When the WSe_2 and Bi_2O_2Se were brought into contact, the higher Fermi level of Bi_2O_2Se would facilitate electrons transfer to WSe_2 until the whole system reaches its thermal equilibrium state with a

unified F_E, which is consisted with the Kelvin probe force microscopy results (Figure S2, Supporting Information). The leaving holes and electrons accumulated at Bi_2O_2Se and WSe_2 side, respectively, formed a built-in potential across the heterojunction impeded further diffusion of the carriers (**Figure 3**d-(i)), which benefits the electrical transmission and photodetection performance by modulating the applied bias, as will be discussed later.

2.3. Electronic Characteristics of WSe_2/Bi_2O_2Se Heterostructure

As construction of heterostructure aims at the suppression of Bi_2O_2Se dark current, we first studied the electrical characterization of WSe_2/Bi_2O_2Se heterostructure in dark as schematically shown in Figure 3a. The voltage (V_{ds}) was applied across the WSe_2 terminal (Drain) to the bottom Bi_2O_2Se (Source) on the SiO_2/Si substrate. Our heterostructure device demonstrated strong rectification behavior with an ideality factor of 1.59 (Figure 3b), indicating good junction interface.[46] The rectification ratio ($|I_{forward}/I_{reverse}|$) increased rapidly, and tended to saturate as the increase of $|V_{ds}|$, ultimately reached to 10^5 when $|V_{ds}| \approx 2$ V, which is competitive among the reported WSe_2-based heterostructure as shown in Figure 3c.[46–50] Such a high rectification ratio can be attributed to the large conduction band offset between Bi_2O_2Se and WSe_2 in Figure 2b.[41,42] The isolated few-layer Bi_2O_2Se and WSe_2 exhibited nearly symmetrical linear curve with electrodes metal (Figure S3, Supporting Information), which rules out the influence of the Schottky barrier for the heterostructure.[25,40] From the transfer curves in Figure S4a, Supporting Information, the intrinsic Bi_2O_2Se demonstrated n-type conductivity with the current increasing from 10^{-7} to 10^{-3} A (V_g from −50 to 50 V), and the WSe_2 demonstrated p-dominant ambipolarity with current varying during 10^{-6} to 10^{-11} A. The carrier concentration and mobility were estimated by n (p) = $q^{-1}C_g|V_{th}|$ = 2.04×10^{12} (1.67×10^{12}) cm^{-2}, and $\mu_{e\,(p)} = \dfrac{\Delta I_{ds}}{\Delta g_s} \times \dfrac{L}{WC_gV_{ds}}$ = 544.8 (2.1) $cm^2\,V^{-1}\,s^{-1}$, where q = 1.6×10^{-9} C, C_g = 1.23×10^{-8} F cm^{-2} for 300 nm SiO_2, $|V_{th}|$ = 25.85 (21.72) V extracted from Figure S4b, Supporting Information, L and W presented the length and width of channel.[34,40,51]
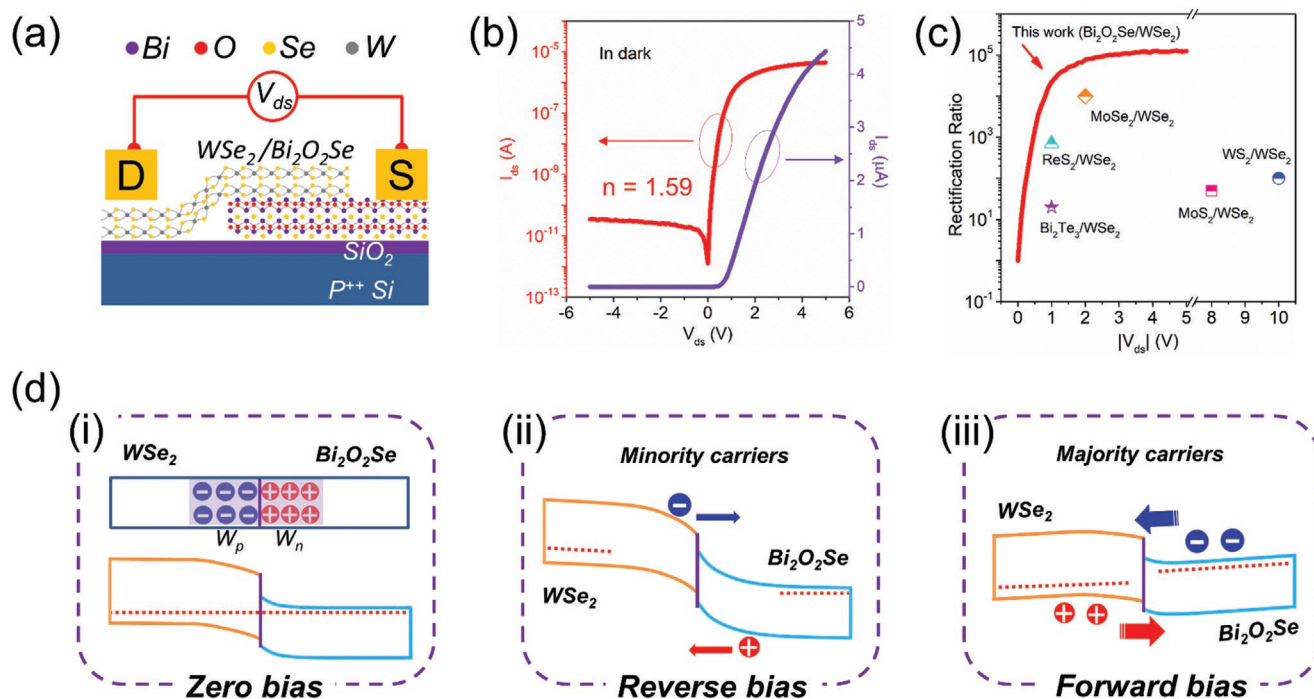
Figure 3. Electronic characteristics of WSe_2/Bi_2O_2Se heterostructure. a) Schematic illustration of WSe_2/Bi_2O_2Se heterostructure diode. b) I–V curves of the heterostructure. c) Comparison of rectification ratio between this work with different diodes reported in literature like MoS_2/WSe_2,[47] WS_2/WSe_2,[48] ReS_2/WSe_2,[49] $MoSe_2/WSe_2$,[50] and Bi_2Te_3/WSe_2.[46] d) Schematic of the band diagrams of WSe_2/Bi_2O_2Se heterostructure under i) zero bias, ii) forward bias, and iii) reverse bias.

On the other hand, the WSe_2/Bi_2O_2Se device presented p-type conductivity dominated ambipolarity in different forward bias similar to WSe_2. The observed carrier transport polarity can be explained by dividing the total resistance of the WSe_2/Bi_2O_2Se heterostructure into three parts: the resistance of overlapped p-n junction, the remaining Bi_2O_2Se and WSe_2 part as shown in the inset of Figure S4c, Supporting Information, since the relatively small contact resistance of metal/Bi_2O_2Se and metal/WSe_2 could be neglected.[41,52] Therefore, the WSe_2/Bi_2O_2Se device exhibited off-state under forward V_g due to the depletion of WSe_2, then switch to on-state under negative V_g due to the accumulation of carriers in both Bi_2O_2Se and WSe_2.

We also take a step further to provide more in-depth insight into the operation of WSe_2/Bi_2O_2Se diode by estimated the depletion width in WSe_2 and Bi_2O_2Se side with the formula:[40,45]

$$x_p = \sqrt{\frac{2N_d\varepsilon_1\varepsilon_2 V_{bi}}{qN_a(\varepsilon_1 N_a + \varepsilon_2 N_d)}} \quad x_n = \sqrt{\frac{2N_a\varepsilon_1\varepsilon_2 V_{bi}}{qN_d(\varepsilon_1 N_a + \varepsilon_2 N_d)}} \quad (1)$$

where the $N_{a\,(d)}$ represents the concentration of the acceptor (donor), which could be calculated by $N_{a(n)} = n\ (p)/t_{Bi2O2Se\,(WSe2)}$, ε_1 and ε_2 are the dielectric constants of Bi_2O_2Se and WSe_2, V_{bi} is the built-in potential at the junction and equals to the difference of work function. According to the thickness $t_{Bi2O2Se\,(WSe2)} = 6.6\ (7.0)$ nm, $\varepsilon_1 = 20$,[29] $\varepsilon_2 = 11.7$,[40] $V_{bi} \approx 0.19$ eV from the UPS test results, the x_p and x_n were calculated about 3.1 and 2.7 nm, indicating the multilayer Bi_2O_2Se and WSe_2 were both undepleted as shown in Figure 3d-(i). When the diode operated under the reverse bias (Figure 3d-(ii)) (i.e., the same direction as the built-in electric field), the potential barrier increased greatly

to block the transportation of majority carriers. As a result, only the minority carriers (holes in Bi_2O_2Se and electrons in WSe_2) could drift across the interface and obtained ultralow reverse current (≈10 pA). On the contrary, when a forward bias was applied in WSe_2 (Figure 3d-(iii)), the decreased potential barrier promoted the majority carriers (electrons in Bi_2O_2Se and holes in WSe_2) to transfer across the junction region easily and obtain large diffusion current.[53,54] It should be noted that a linear region with negative slope was found in the $\ln(I_{ds}/V_{ds}^2)$ against $1/V_{ds}$ plot (Figure S5, Supporting Information), which matched well with the Fowler–Nordheim (FN) tunneling equation $\left(I \propto V^2 exp\left(\frac{-4d\sqrt{2m^*\phi^3}}{3\hbar qV}\right)\right)$ and evidenced the contribution of FN tunneling current under the forward bias[49] due to the high doping concentration.[40,55]

2.4. Photoresponse Properties of WSe_2/Bi_2O_2Se Heterostructure

Taking advantage of the good rectification property and low reverse current, we further explored the optoelectronic characteristics of the WSe_2/Bi_2O_2Se heterostructure without gate voltage. When the light (532 nm) illuminated on the device, the photogenerated electrons and holes in both Bi_2O_2Se layer and WSe_2 layer were expected to separate and transfer into different materials by the built-in electric field at the interface (inset of **Figure 4**a). These charge carries transferred laterally between electrodes and contributed an additional current which called photocurrent I_{ph} (The difference between I_{ds} with and without illumination). Figure 4a presents the I–V curves on a logarithmic scale under dark and different power intensity of
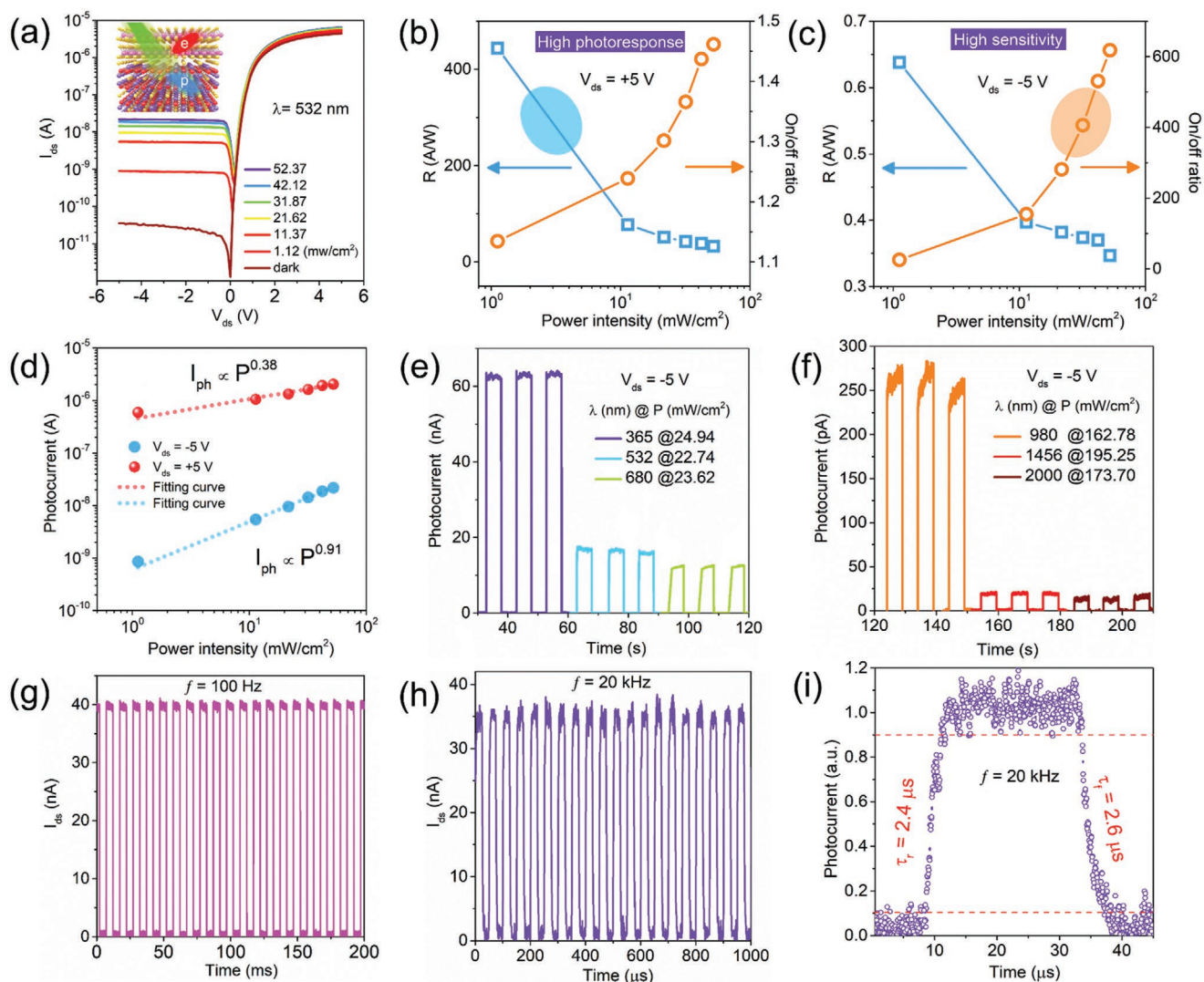
Figure 4. Photoresponse characteristics of WSe$_2$/Bi$_2$O$_2$Se heterostructure. a) I_{ds}–V_{ds} measurements under different laser powers intensity of 532 nm for WSe$_2$/Bi$_2$O$_2$Se heterostructure, inset: schematic diagram of the separation process of photogenerated carries on the interface of WSe$_2$/Bi$_2$O$_2$Se heterostructure under laser illumination. b,c) Responsivity and light on/off ratio of WSe$_2$/Bi$_2$O$_2$Se heterostructure under varied light intensities at V_{ds} = +5 V and V_{ds} = −5 V, separately. d) The photocurrent dependence of laser power intensity at V_{ds} = −5 V and +5 V. e,f) Photoresponse of the heterostructure under different visible light wavelengths (365, 532, and 680 nm) and shortwave infrared light wavelengths (980, 1456, 2000 nm) at V_{ds} = −5 V. g,h) Photoresponse of the heterostructure under 532 nm with a frequency of 100 Hz and 20 kHz at V_{ds} = −5 V. i) Rise and decay curves of the heterostructure under 532 nm (20 kHz) at V_{ds} = −5 V.

532 nm light from −5 to +5 V. Apparently, the device maintained good rectifying characteristics under illumination and presented distinct photoresponse characteristics at reverse and forward bias. When the V_{ds} > 0, the device operated in on-state, a large number of free carriers could across the heterostructure and contributed to the overall current, thus the light induced electron-hole pairs only took a small part (i.e., a low light on/off ratio). On the other hand, when the V_{ds} < 0, the device worked in off-state and the photogenerated carriers became dominated. Therefore, the photocurrent was much higher than the dark current, and high sensitivity photodiode with a significant light on/off ratio was obtained. Furthermore, we calculated the responsivity (R) of the WSe$_2$/Bi$_2$O$_2$Se heterostructure device with the formula $R = I_{ph}/PS$, where S is the active area

of illumination.[56] When V_{ds} = +5 V in Figure 4b, a high photoresponsivity with R = 443.83 A W^{-1} (532 nm @ 1.12 mW cm^{-2}) was achieved, which is competitive in most intrinsic 2D metal chalcogenides and their vdW photodetectors.[37] On the contrary, when WSe$_2$/Bi$_2$O$_2$Se heterostructure device operated under −5 V as shown in Figure 4c, the light on/off ratio enhanced to 618 (532 nm @ 52.37 mW cm^{-2}) and a decent photoresponsivity of 638 mA W^{-1} (1.12 mW cm^{-2}) in the WSe$_2$/Bi$_2$O$_2$Se photodiode is also comparable to those of reported literature.[41,43,47,52,57] By fitting the light intensity (P) dependent I_{ph} through the equation of $I_{ph} \propto P^\alpha$ (Figure 4d), it was found that I_{ph} at V_{ds} = +5 V was relatively larger than 10^{-6} A level with the α = 0.38, which indicated the existence of photogating effect and high photogain.[34] Therefore, the WSe$_2$/Bi$_2$O$_2$Se heterostructure could
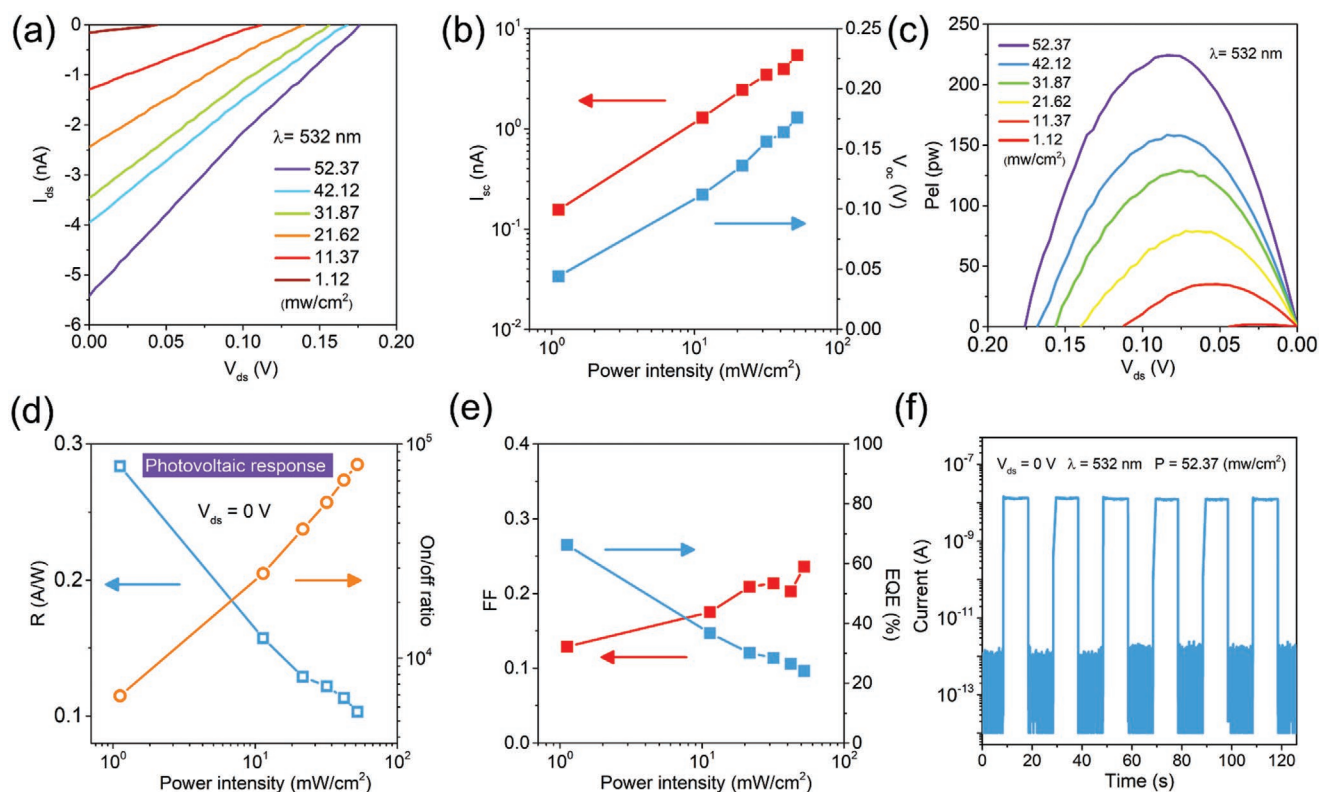
**ADVANCED
SCIENCE NEWS**
www.advancedsciencenews.com

**ADVANCED
FUNCTIONAL
MATERIALS**
www.afm-journal.de

Figure 5. Self-driven photoresponse characterization of WSe_2/Bi_2O_2Se heterostructure. a) Enlarged I_{ds}–V_{ds} measurements of Figure 4a. b) Extracted I_{sc} and V_{oc} under different laser powers intensity of 532 nm. c) Electrical power generated by the WSe_2/Bi_2O_2Se heterostructure as a function of V_{ds}. d) Responsivity and light on/off ratio of WSe_2/Bi_2O_2Se heterostructure under varied power intensities at $V_{ds} = 0$ V. e) FF and EQE as a function of laser powers intensity under 532 nm. f) Time-resolved photovoltaic response of the heterostructure under 532 nm at $V_{ds} = 0$ V.

operate as photodiode with high photoresponse and high sensitivity as the photoswitching characterization in Figure S6a,b, Supporting Information. With the increase of power intensity of 532 nm light, the photoresponse of the photodiode kept increasing while the dark current maintained relatively low when $V_{ds} = -5$ V, which outperformed the intrinsic Bi_2O_2Se based photodetector with high dark current.[25,32,36]

The ultra-low dark current and remarkable photoresponse of the WSe_2/Bi_2O_2Se photodiode also provided a platform for the broadband photodetection. As shown in Figure 4e,f, the WSe_2/Bi_2O_2Se photodiode demonstrated rapid and stable photoresponse from 365 to 2000 nm. It should be noted that the photoresponse at 2000 nm was beyond their individual response range, which may be attributed to the interlayer coupling of Bi_2O_2Se and WSe_2.[58,59] Furthermore, we measured the response speed of the WSe_2/Bi_2O_2Se heterostructure by varying the laser switching frequency from 100 Hz to 20 kHz (equipment limit) and found no significant current decay at higher frequency as demonstrated in Figure 4g,h and Figure S7, Supporting Information, which indicated the frequency bandwidth is much higher than 20 kHz. Therefore, we estimated the frequency bandwidth (f_{3dB}) of the heterostructure from the response time $\tau = 0.55/f_{3dB}$.[49] Since the rise time was 2.4 µs and the fall time was 2.6 µs (Figure 4i), the frequency bandwidth of WSe_2/Bi_2O_2Se heterostructure was calculated $\approx 10^5$ Hz.

When focusing on photoresponse around zero bias, we found the WSe_2/Bi_2O_2Se heterostructure also exhibited

excellent self-driven properties. **Figure 5**a zooms in the I–V curves of Figure 4a, in which obvious photovoltaic response is presented with the curves pass across the four quadrants. When the WSe_2/Bi_2O_2Se heterostructure was illuminated by 532 nm laser in open circuit, photogenerated electron-hole pairs could separate rapidly by build-in potential and drift to different side layers (electrons to Bi_2O_2Se, holes to WSe_2). The accumulated electrons and holes in Bi_2O_2Se layers and WSe_2 layers broke the thermal equilibrium of dark state and formed forward open circuit voltage (V_{oc}). Once the device was short circuited, the separated photogenerated carries could recombine and result in short circuit current (I_{sc}). Figure 5b demonstrates the V_{oc} and I_{sc} both monotonically increased with the light power intensity without reaching a saturation. The V_{oc} followed a logarithmic dependence on the intensity and I_{sc} followed a linear dependence, indicating the good photovoltaic effect dominated the photocurrent generation.[56] The electrical power (P_{el}) generated by the WSe_2/Bi_2O_2Se device under various power intensity was extracted by the formula $P_{el} = I_{ds}V_{ds}$ (Figure 5c). The P_{el} increased with the light power intensity and reached 224 pW when $P = 52.37$ mW cm^{-2}. The transient photovoltaic response of 532 nm under varied light intensities (Figure S8, Supporting Information) demonstrated a stable ultralow dark current (10^{-13} A) and provided a high light on/off ratio around 10^5. What's more, the photovoltaic responsivity is up to 284 mA W^{-1} when the WSe_2/Bi_2O_2Se device operated under 1.12 mW cm^{-2} as shown in Figure 5d. On the other hand, we calculated the

**ADVANCED
SCIENCE NEWS**

www.advancedsciencenews.com

**ADVANCED
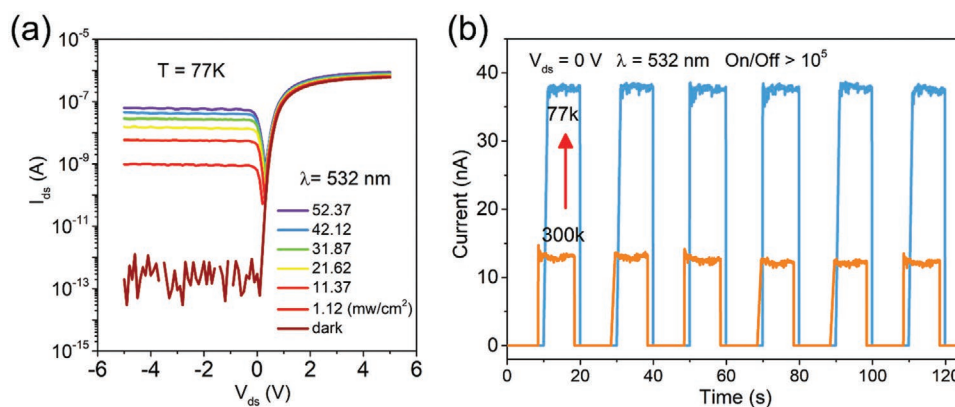FUNCTIONAL
MATERIALS**

www.afm-journal.de

Figure 6. Low temperature performance of WSe_2/Bi_2O_2Se heterostructure as the photoelectric and photovoltaic devices. a) I_{ds}–V_{ds} characteristics under different light irradiation powers for WSe_2/Bi_2O_2Se heterostructure at 77 K. b) Photovoltaic response under 77 and 300 K.

important indicators of photovoltaic energy conversion: fill factor (FF) and external quantum efficiency (EQE) for our WSe_2/Bi_2O_2Se self-driven detector by the formula: FF $= P_{el,max}/(I_{sc}V_{oc})$ and EQE $= (I_{ph}/P)(hc/q\lambda) = R(hc/q\lambda)$ (where h is the Planck constant, q is the unit charge and λ is the excitation wavelength).[41,60] From the Figure 5e, the WSe_2/Bi_2O_2Se heterostructure obtained maximum FF of 0.24 and EQE up to 66.27% under 52.27 and 1.12 mW cm^{-2}, respectively, which is comparable to reported values based on MoS_2/WSe_2 (1.5%, 34%),[47,59] MoS_2/BP (0.3%)[41] and AsP/InSe (1.5%).[42] The power conversion efficiency defined as $\eta_{PV} = P_{el}/P_{in}$ was calculated $\approx 0.428\%$ under 52.27 mW cm^{-2}. The periodically switched photocurrent without severe degradation (Figure 5f) guaranteed the good stability and reproducibility for the photovoltaic response of our WSe_2/Bi_2O_2Se heterostructure device with the response speed about 20 µs.

The electrical transport and photoelectric detection performance of WSe_2/Bi_2O_2Se heterostructure could be further improved at low temperature (77 K). As shown in **Figure 6**a, the forward dark current at 77 K slightly decreased compared to the case at room temperature due to the suppressed thermal emission and lower carrier density.[32] The two-order of magnitudes smaller current at reverse dark current (10^{-13} A) indicates the enlarged build-in potential at the interface of WSe_2/Bi_2O_2Se at low temperature.[61] The ultra-low reverse dark current not only magnified the rectification ratio of WSe_2/Bi_2O_2Se diode to 10^7, but also increased the light on/off ratio of the photodiode to nearly 10^6, which were among the highest value ever reported in two-terminal device without gate modulation.[42] Besides, the WSe_2/Bi_2O_2Se photovoltaic response in 77 K (Figure 6b) demonstrated a higher I_{ph} comparing to the result at room temperature due to more effective separation of photogenerated carries in the strengthened build-in potential.[61]

The comparison of performance between our WSe_2/Bi_2O_2Se heterostructure with individual Bi_2O_2Se and other reported 2D vdW heterostructure is shown in Table S1, Supporting Information. The dark current of our WSe_2/Bi_2O_2Se photodiode was greatly suppressed by more than four orders of magnitudes compared to reported 2D Bi_2O_2Se photodetector, which is significant for low power consumption in practical applications. The light on/off ratio and response speed were both improved due to large built-in barrier and fast separation of photogenerated

carriers at the interface of Bi_2O_2Se and WSe_2.[62] Meanwhile, the high electron mobility and novel optoelectronics properties of 2D Bi_2O_2Se[16,25] also contributed to the excellent photodetection performance of our WSe_2/Bi_2O_2Se heterostructure device compared to other 2D vdW heterostructure.

3. Conclusion

In summary, a WSe_2/Bi_2O_2Se p-n heterostructure with type-II band alignment has been constructed to improve the photodetection performance of 2D Bi_2O_2Se nanosheet. Strong interlayer coupling effect and large interfacial band offset between WSe_2 and Bi_2O_2Se were verified by UPS, Raman, and PL tests, which provided high rectification characteristics with a ratio up to 10^5 and a low dark current of 10^{-11} A. As a result, the photodetector shows a decent responsivity of 638 mA W^{-1}, a high light on/off ratio of 618, fast response speed of 2.6 µs, and broadband photodetection from 365 to 2000 nm. More importantly, the self-driven photodetection was first achieved in WSe_2/Bi_2O_2Se heterostructure with a light on/off ratio up to 10^5 and a responsivity of 284 mA W^{-1}. Ultra-low reverse current about 10^{-13} A at low temperature (77 K) further improved the performance of the WSe_2/Bi_2O_2Se backward diode and photodetecor. The proposed 2D WSe_2/Bi_2O_2Se heterostructure extends the promising potentials of Bi_2O_2Se in the self-driven, high sensitivity, broadband, and fast photodetection.

4. Experimental Section

Device Fabrication of 2D WSe_2/Bi_2O_2Se Heterostructure: 2D Bi_2O_2Se was first synthesized on mica by CVD method in which the source Bi_2O_3 powder and Bi_2Se_3 power were placed in the hot center and 6 cm upstream of a tube furnace, respectively, and mica substrates were placed in 12–15 cm downstream. The center temperature of the tube furnace was set about 680–750 °C with ramping time about 30 min and hold time of 25 min, and final cooled to room temperature naturally. The high purity Ar gas was used to evacuate the ambient contamination of the quartz tube with high flow before heating, and then acted as carrier gas at 200 sccm during the whole growth process. Then, the prepared Bi_2O_2Se was transferred from mica to SiO_2/Si substrate by a wet transfer method supporting by poly methyl methacrylate in a dilute HF solution (1%) and final cleaned by acetone. The 2D WSe_2 was exfoliated

on a PDMS transparent stamp and transferred to the top of prepared Bi_2O_2Se nanosheet on SiO_2/Si substrate by micromanipulation transfer system equipped OM. Finally, the contact electrodes were patterned by standard electron-beam lithography (FEI Quanta 650 scanning electron microscope and Raith Elphy Plus) and deposited with Cr/Au (5/50 nm) metal by a thermally evaporating system (Nexdep, Angstrom Engineering).

Characterization: The fabricated WSe_2/Bi_2O_2Se heterostructure was characterized by OM (BX51, OLMPUS), the thickness and surface potential difference were evaluated by atomic force microscope (Dimension Icon, Bruker), the Raman and PL spectra were both measured by a confocal microscope spectrometer (Alpha 300R, WITec). The energy band alignment was tested by UPS (Axis Ultra DLD, Kratos). The electronic and photodetection measurement were carried out by semiconductor analyzer (B1500A, Agilent) and probe station (TTPX, Lakeshore) under illumination of laser sources (365, 532, 680, 980, 1456, and 2000 nm) with adjustable power intensity which were calibrated by powermeter (FieldMaxII-TO, Coherent).

Supporting Information

Supporting Information is available from the Wiley Online Library or from the author.

Conflict of Interest

The authors declare no conflict of interest.

[1] N. Mounet, M. Gibertini, P. Schwaller, D. Campi, A. Merkys, A. Marrazzo, T. Sohier, I. E. Castelli, A. Cepellotti, G. Pizzi, N. Marzari, *Nat. Nanotechnol.* **2018**, *13*, 246.

[2] F. H. Koppens, T. Mueller, P. Avouris, A. C. Ferrari, M. S. Vitiello, M. Polini, *Nat. Nanotechnol.* **2014**, *9*, 780.

[3] N. Huo, G. Konstantatos, *Adv. Mater.* **2018**, *30*, 1801164.

[4] W. Han, P. Huang, L. Li, F. Wang, P. Luo, K. Liu, X. Zhou, H. Li, X. Zhang, Y. Cui, T. Zhai, *Nat. Commun.* **2019**, *10*, 4728.

[5] K. S. Novoselov, A. K. Geim, S. V. Morozov, D. Jiang, Y. Zhang, S. V. Dubonos, I. V. Grigorieva, A. A. Firsov, *Science* **2004**, *306*, 666.

[6] B. Y. Zhang, T. Liu, B. Meng, X. Li, G. Liang, X. Hu, Q. J. Wang, *Nat. Commun.* **2013**, *4*, 1811.

[7] T. Mueller, F. N. A. Xia, P. Avouris, *Nat. Photonics* **2010**, *4*, 297.

[8] L. Li, Y. Yu, G. J. Ye, Q. Ge, X. Ou, H. Wu, D. Feng, X. H. Chen, Y. Zhang, *Nat. Nanotechnol.* **2014**, *9*, 372.

[9] Z. Zhang, L. Li, J. Horng, N. Z. Wang, F. Yang, Y. Yu, Y. Zhang, G. Chen, K. Watanabe, T. Taniguchi, X. H. Chen, F. Wang, Y. Zhang, *Nano Lett.* **2017**, *17*, 6097.

[10] L. Li, W. Han, L. Pi, P. Niu, J. Han, C. Wang, B. Su, H. Li, J. Xiong, Y. Bando, T. Zhai, *InfoMat* **2019**, *1*, 54.

[11] Y. Fang, Q. Dong, Y. Shao, Y. Yuan, J. Huang, *Nat. Photonics* **2015**, *9*, 679.

[12] F. Li, C. Ma, H. Wang, W. Hu, W. Yu, A. D. Sheikh, T. Wu, *Nat. Commun.* **2015**, *6*, 8238.

[13] W. Wang, D. Zhao, F. Zhang, L. Li, M. Du, C. Wang, Y. Yu, Q. Huang, M. Zhang, L. Li, J. Miao, Z. Lou, G. Shen, Y. Fang, Y. Yan, *Adv. Funct. Mater.* **2017**, *27*, 1703953.

[14] K. F. Mak, J. Shan, *Nat. Photonics* **2016**, *10*, 216.

[15] S.-S Wang, X.-X. Chen, B. Huang, R.-K Huang, W.-X Zhang, X.-M Chen, *CCS Chem.* **2019**, *1*, 448.

[16] J. Wu, H. Yuan, M. Meng, C. Chen, Y. Sun, Z. Chen, W. Dang, C. Tan, Y. Liu, J. Yin, Y. Zhou, S. Huang, H. Q. Xu, Y. Cui, H. Y. Hwang, Z. Liu, Y. Chen, B. Yan, H. Peng, *Nat. Nanotechnol.* **2017**, *12*, 530.

[17] C. Chen, M. Wang, J. Wu, H. Fu, H. Yang, Z. Tian, T. Tu, H. Peng, Y. Sun, X. Xu, J. Jiang, N. B. M. Schroter, Y. Li, D. Pei, S. Liu, S. A. Ekahana, H. Yuan, J. Xue, G. Li, J. Jia, Z. Liu, B. Yan, H. Peng, Y. Chen, *Sci. Adv.* **2018**, *4*, eaat8355.

[18] M. Wu, X. C. Zeng, *Nano Lett.* **2017**, *17*, 6309.

[19] Q. Wei, R. Li, C. Lin, A. Han, A. Nie, Y. Li, L. J. Li, Y. Cheng, W. Huang, *ACS Nano* **2019**, *13*, 13439.

[20] J. Wu, C. Tan, Z. Tan, Y. Liu, J. Yin, W. Dang, M. Wang, H. Peng, *Nano Lett.* **2017**, *17*, 3021.

[21] J. Wu, C. Qiu, H. Fu, S. Chen, C. Zhang, Z. Dou, C. Tan, T. Tu, T. Li, Y. Zhang, Z. Zhang, L. M. Peng, P. Gao, B. Yan, H. Peng, *Nano Lett.* **2019**, *19*, 197.

[22] U. Khan, Y. Luo, L. Tang, C. Teng, J. Liu, B. Liu, H. M. Cheng, *Adv. Funct. Mater.* **2019**, *29*, 1807979.

[23] Z. Wu, G. Liu, Y. Wang, X. Yang, T. Wei, Q. Wang, J. Liang, N. Xu, Z. Li, B. Zhu, H. Qi, Y. Deng, J. Zhu, *Adv. Funct. Mater.* **2019**, *29*, 1906639.

[24] J. Wu, Y. Liu, Z. Tan, C. Tan, J. Yin, T. Li, T. Tu, H. Peng, *Adv. Mater.* **2017**, *29*, 1704060.

[25] Q. Fu, C. Zhu, X. Zhao, X. Wang, A. Chaturvedi, C. Zhu, X. Wang, Q. Zeng, J. Zhou, F. Liu, B. K. Tay, H. Zhang, S. J. Pennycook, Z. Liu, *Adv. Mater.* **2019**, *31*, 1804945.

[26] C. Tan, M. Tang, J. Wu, Y. Liu, T. Li, Y. Liang, B. Deng, Z. Tan, T. Tu, Y. Zhang, C. Liu, J. H. Chen, Y. Wang, H. Peng, *Nano Lett.* **2019**, *19*, 2148.

[27] Y. Liang, Y. Chen, Y. Sun, S. Xu, J. Wu, C. Tan, X. Xu, H. Yuan, L. Yang, Y. Chen, P. Gao, J. Guo, H. Peng, *Adv. Mater.* **2019**, *31*, 1901964.

[28] X. Tian, H. Luo, R. Wei, C. Zhu, Q. Guo, D. Yang, F. Wang, J. Li, J. Qiu, *Adv. Mater.* **2018**, *30*, 1801021.

[29] T. Ghosh, M. Samanta, A. Vasdev, K. Dolui, J. Ghatak, T. Das, G. Sheet, K. Biswas, *Nano Lett.* **2019**, *19*, 5703.

[30] J. Yang, R. Quhe, Q. Li, S. Liu, L. Xu, Y. Pan, H. Zhang, X. Zhang, J. Li, J. Yan, B. Shi, H. Pang, L. Xu, Z. Zhang, J. Lu, J. Yang, *Adv. Electron. Mater.* **2019**, *5*, 1800720.

[31] Z. Zhang, T. Li, Y. Wu, Y. Jia, C. Tan, X. Xu, G. Wang, J. Lv, W. Zhang, Y. He, J. Pei, C. Ma, G. Li, H. Xu, L. Shi, H. Peng, H. Li, *Adv. Mater.* **2019**, *31*, 1805769.

[32] J. Li, Z. X. Wang, Y. Wen, J. W. Chu, L. Yin, R. Q. Cheng, L. Lei, P. He, C. Jiang, L. P. Feng, J. He, *Adv. Funct. Mater.* **2018**, *28*, 1706437.

[33] J. Yin, Z. Tan, H. Hong, J. Wu, H. Yuan, Y. Liu, C. Chen, C. Tan, F. Yao, T. Li, Y. Chen, Z. Liu, K. Liu, H. Peng, *Nat. Commun.* **2018**, *9*, 3311.

**ADVANCED
SCIENCE NEWS**

www.advancedsciencenews.com

**ADVANCED
FUNCTIONAL
MATERIALS**

www.afm-journal.de

[34] P. Luo, F. Zhuge, F. Wang, L. Lian, K. Liu, J. Zhang, T. Zhai, *ACS Nano* **2019**, *13*, 9028.

[35] T. Tong, Y. Chen, S. Qin, W. Li, J. Zhang, C. Zhu, C. Zhang, X. Yuan, X. Chen, Z. Nie, X. Wang, W. Hu, F. Wang, W. Liu, P. Wang, X. Wang, R. Zhang, Y. Xu, *Adv. Funct. Mater.* **2019**, *29*, 1905806.

[36] H. Yang, C. Tan, C. Deng, R. Zhang, X. Zheng, X. Zhang, Y. Hu, X. Guo, G. Wang, T. Jiang, Y. Zhang, G. Peng, H. Peng, X. Zhang, S. Qin, *Small* **2019**, *15*, 1904482.

[37] X. Zhou, X. Z. Hu, J. Yu, S. Y. Liu, Z. W. Shu, Q. Zhang, H. Q. Li, Y. Ma, H. Xu, T. Y. Zhai, *Adv. Funct. Mater.* **2018**, *28*, 1706587.

[38] Y. Zhang, Y. Yao, M. G. Sendeku, L. Yin, X. Zhan, F. Wang, Z. Wang, J. He, *Adv. Mater.* **2019**, *31*, 1901694.

[39] C. Zhang, C. Gong, Y. Nie, K.-A. Min, C. Liang, Y. J. Oh, H. Zhang, W. Wang, S. Hong, L. Colombo, R. M. Wallace, K. Cho, *2D Mater.* **2016**, *4*, 015026.

[40] X. Zhou, X. Hu, S. Zhou, H. Song, Q. Zhang, L. Pi, L. Li, H. Li, J. Lu, T. Zhai, *Adv. Mater.* **2018**, *30*, 1703286.

[41] Y. Deng, Z. Luo, N. J. Conrad, H. Liu, Y. Gong, S. Najmaei, P. M. Ajayan, J. Lou, X. Xu, P. D. Ye, *ACS Nano* **2014**, *8*, 8292.

[42] F. Wu, H. Xia, H. Sun, J. Zhang, F. Gong, Z. Wang, L. Chen, P. Wang, M. Long, X. Wu, J. Wang, W. Ren, X. Chen, W. Lu, W. Hu, *Adv. Funct. Mater.* **2019**, *29*, 1900314.

[43] S. Yang, K. Liu, W. Han, L. Li, F. Wang, X. Zhou, H. Li, T. Zhai, *Adv. Funct. Mater.* **2019**, *30*, 1908382.

[44] B. Peng, G. Yu, X. Liu, B. Liu, X. Liang, L. Bi, L. Deng, T. C. Sum, K. P. Loh, *2D Mater.* **2016**, *3*, 025020.

[45] M. H. Doan, Y. Jin, S. Adhikari, S. Lee, J. Zhao, S. C. Lim, Y. H. Lee, *ACS Nano* **2017**, *11*, 3832.

[46] H. Liu, X. Zhu, X. Sun, C. Zhu, W. Huang, X. Zhang, B. Zheng, Z. Zou, Z. Luo, X. Wang, D. Li, A. Pan, *ACS Nano* **2019**, *13*, 13573.

[47] M. M. Furchi, A. Pospischil, F. Libisch, J. Burgdorfer, T. Mueller, *Nano Lett.* **2014**, *14*, 4785.

[48] N. Huo, J. Yang, L. Huang, Z. Wei, S. S. Li, S. H. Wei, J. Li, *Small* **2015**, *11*, 5430.

[49] A. Varghese, D. Saha, K. Thakar, V. Jindal, S. Ghosh, N. V. Medhekar, S. Ghosh, S. Lodha, *Nano Lett.* **2020**, *20*, 1707.

[50] H. Xue, Y. Wang, Y. Dai, W. Kim, H. Jussila, M. Qi, J. Susoma, Z. Ren, Q. Dai, J. Zhao, K. Halonen, H. Lipsanen, X. Wang, X. Gan, Z. Sun, *Adv. Funct. Mater.* **2018**, *28*, 1804388.

[51] L. Lv, F. Zhuge, F. Xie, X. Xiong, Q. Zhang, N. Zhang, Y. Huang, T. Zhai, *Nat. Commun.* **2019**, *10*, 3331.

[52] F. Wang, L. Yin, Z. X. Wang, K. Xu, F. M. Wang, T. A. Shifa, Y. Huang, C. Jiang, J. He, *Adv. Funct. Mater.* **2016**, *26*, 5499.

[53] Y. Chen, X. Wang, G. Wu, Z. Wang, H. Fang, T. Lin, S. Sun, H. Shen, W. Hu, J. Wang, J. Sun, X. Meng, J. Chu, *Small* **2018**, *14*, 1703293.

[54] N. Huo, J. Kang, Z. Wei, S.-S. Li, J. Li, S.-H. Wei, *Adv. Funct. Mater.* **2014**, *24*, 7025.

[55] F. Wang, P. Luo, Y. Zhang, Y. Huang, Q. Zhang, Y. Li, T. Zhai, *Sci. China Mater.* **2020**, *63*, 1537.

[56] D. J. Groenendijk, M. Buscema, G. A. Steele, S. M. de Vasconcellos, R. Bratschitsch, H. S. J. van der Zant, A. Castellanos-Gomez, *Nano Lett.* **2014**, *14*, 5846.

[57] L. H. Zeng, S. H. Lin, Z. J. Li, Z. X. Zhang, T. F. Zhang, C. Xie, C. H. Mak, Y. Chai, S. P. Lau, L. B. Luo, Y. H. Tsang, *Adv. Funct. Mater.* **2018**, *28*, 1705970.

[58] G. Wang, L. Li, W. Fan, R. Wang, S. Zhou, J.-T. Lü, L. Gan, T. Zhai, *Adv. Funct. Mater.* **2018**, *28*, 1800339.

[59] C. H. Lee, G. H. Lee, A. M. van der Zande, W. Chen, Y. Li, M. Han, X. Cui, G. Arefe, C. Nuckolls, T. F. Heinz, J. Guo, J. Hone, P. Kim, *Nat. Nanotechnol.* **2014**, *9*, 676.

[60] W. Deng, C. You, X. Chen, Y. Wang, Y. Li, B. Feng, K. Shi, Y. Chen, L. Sun, Y. Zhang, *Small* **2019**, *15*, 1901544.

[61] F. Wang, Z. Wang, K. Xu, F. Wang, Q. Wang, Y. Huang, L. Yin, J. He, *Nano Lett.* **2015**, *15*, 7558.

[62] W. H. Wu, Q. Zhang, X. Zhou, L. Li, J. W. Su, F. K. Wang, T. Y. Zhai, *Nano Energy* **2018**, *51*, 45.